PHYSICAL REVIEW FLUIDS **3**, 094606 (2018)

Mean kinetic energy replenishment mechanisms in vertical-axis wind turbine farms

Seyed Hossein Hezaveh and Elie Bou-Zeid[*]
Department of Civil and Environmental Engineering, Princeton University, Princeton, New Jersey 08544, USA

(Received 16 June 2017; published 26 September 2018)

Vertical-axis wind turbines (VAWTs) are the subject of renewed interest due to the potential for higher power generation per unit land used, as well as their lower center of mass (the generator is at the bottom of tower), which renders them favorable for offshore deployment. However, VAWT farms have hardly been studied. In this paper, using a previously tested actuator line model in a large eddy simulation code, we investigate the transport of the mean kinetic energy (MKE) that replenishes the power in the farm. The primary sources of MKE are (1) the initial advective streamwise influx through the frontal area and (2) the vertical planform influx through the top and bottom interfaces of the farm. The results show that, for realistic finite-size farms, the planform MKE transport is a loss term over the first six rows: in this initial zone the mean flow adjusts by slowing down, and an upward mean advection develops that results in an efflux loss of MKE from the farm volume. The power extracted from farms is thus mainly from the frontal advection over the first few rows. When the initial streamwise advective flux is exhausted, the planform regeneration of MKE from above the wind farm becomes the dominant source; it is primarily affected by turbulent-mean interaction. This regeneration continues to adjust until rows 8 to 10 in our setups, beyond which a fully developed flow (similar to an infinite wind farm) can be observed. In the fully developed region, actual mechanical power generation by the turbines is about one third of replenishment. A primary conclusion is that more irregular farms designs should be studied, while the current literature continues to focus on the very classic layouts.

DOI: 10.1103/PhysRevFluids.3.094606

I. INTRODUCTION

The current power density of wind farms, defined as the power generation per unit land used, is on the order of $2\,\mathrm{W/m^2}$ (assuming a hub height wind speed of $6\,\mathrm{m\,s^{-1}}$) [1]. This is a rather low density, but its disadvantages are partially mitigated by other uses that land area between individual turbines can have (e.g., many current farms lease small areas for the tower base in agricultural lands). Therefore, this has not been a significant detriment for wind energy expansion in the past. However, to reach penetration rates into the electric market that would reverse the continuously rising greenhouse gas emissions, the cumulative installed capacities around the world must increase significantly. The US goal of 20% electricity from wind by 2030, for example, requires the installed capacity to reach 300 GW as outlined by the Department of Energy [2], whereas by the end of 2017 this capacity was only about 85 GW. Reaching the future goals hence entails a significant expansion of wind farms, raising the need for land (and the price in windy locations) and potentially forcing expansion into regions with less favorable wind meteorology. This future path increases the appeal of higher density farm configurations, as well as offshore deployments. Higher densities also reduce

---

[*] Corresponding author: ebouzeid@princeton.edu

the need for longer transmission lines on the farm and other logistical challenges associated with maintenance, which is of particular appeal for offshore installations.

To reach such higher power densities, innovative farm designs are needed. As proposed and illustrated by Dabiri [3], vertical axis wind turbines (VAWTs) can be arranged in configurations to allow synergistic interactions between the turbines, enabling closer spacing in a farm. This was shown by Hezaveh *et al.* [4] to increase the power output and average power coefficient (C_P) values for the whole wind farm per unit land used by about 22% when clusters of three turbines each are used as the farm building blocks. In that previous assessment however, infinite wind farms were simulated using periodic boundary conditions in the numerical configuration. Infinite farms are proxies for extensively large wind farms in which the front rows (where the flow is adjusting to the new roughness) have a limited impact on the total farm output, and as such the mean and turbulence can be considered horizontally homogenous over most of the farm area. This infinite wind farm setup is also very common in simulations of horizontal axis wind turbine (HAWT) farms [5–8]. Those simulations hence are only representative of very large farms where the wind farm boundary layer is fully developed, and where the frontal power that is streamwise-advected into the farm through the frontal area plays a minor role. In such configurations, only the downward flux of energy across the plane spanning the turbine rotors vertices is available to replenish the MKE of the air inside the farm and to sustain energy production, as discussed by Dabiri *et al.* [3]. This downward transfer of MKE is thus the upper limit on power extraction by HAWT or VAWT arrays in very large farms, unlike a single standing turbine or a small farm where the frontal streamwise advected power controls the maximum potential generation.

Calaf *et al.* [5] addressed these same challenges for HAWT wind farms; they found that farms with a horizontal length larger than 10–20 km (an order of magnitude larger than the typical ABL height) will reach this infinite length wind farm regime (though this should formally be expressed in terms of the length normalized by the turbine diameter). They also simulated various HAWT configurations and investigated the effect and magnitude of different kinetic energy transport mechanisms in such fully developed boundary layer regimes. Their findings indicate that vertical fluxes of MKE have the same order of magnitude as the power extracted by the wind turbines, confirming that this flux is the main source of MKE for the farm. This implies that the minimal allowable proximity of turbines in such infinite farms is limited by the downward replenishment of MKE per unit area. Due to the ability of VAWTs to be placed in closer proximity to raise power density as demonstrated recently for large farms by Hezaveh *et al.* [4], questions arise as to the limits on such proximity that might be imposed by the constraint of MKE replenishment, and whether even closer arrangements can be used in farms with limited fetch. Fetch in this paper is defined as the full length of the farm in the streamwise direction.

Using a previously validated actuator line model (ALM) large eddy simulation (LES) code for VAWT wind farms, in this study, we perform simulations on finite and infinite fetch (periodic) wind farms and investigate the mechanisms responsible for kinetic energy replenishment and power recovery in these farms, and how they evolve with distance from the upwind leading edge of the farm (defined as streamwise distance from the very first row). The need to examine MKE replenishment and optimal turbine spacing specifically in the context of VAWTs (rather than adopt HAWT results) arises since the wakes and interturbine interactions for these machines are significantly different from their HAWTs counterparts, and since significantly higher VAWT farm densities (relative to the literature on HAWT farms) are being proposed. However, previous studies on VAWT farm energy budgets remain limited. Kinzel *et al.* [9] investigated such budgets using field experiments, which limited the scale of the farm and the range of flow information they could access.

We will compare large "infinite" wind farms and finite ones to answer the following research questions: (1) What transport mechanisms dominate the regeneration of MKE in VAWT wind farms, and how do they vary with the distance from the leading edge? (2) How large should VAWT wind farms be to display the dynamics of fully developed (infinite) wind-turbine array boundary layers?

II. NUMERICAL MODEL

To investigate VAWTs in the ABL, a validated LES code with an actuator line model (ALM-LES) [4,10] is used. The filtered Navier-Stokes equations are explicitly solved for the large scales using a pseudospectral approach in the horizontal directions (filtering and gradient computations are done in Fourier space) and second-order centered differencing in the vertical direction. The effect of the subgrid scale (SGS) eddies on the resolved scales is modeled using a scale-dependent Lagrangian dynamic subgrid scale model [11], and the second order Adams-Bashforth scheme is used for time integration. The effect of VAWTs on the ABL flow is represented as horizontal forces imposed by the blades at each time step in each grid cell where a blade element is present (and some adjacent cells). These forces are added to the filtered Navier-Stokes equations, solved here in rotational form but without Coriolis (its impact on farm scale flow dynamics is not significant) or buoyancy forces, to yield

$$\frac{\partial \tilde{u}_i}{\partial x_i} = 0, \tag{1}$$

$$\frac{\partial \tilde{u}_i}{\partial t} + \tilde{u}_j\left(\frac{\partial \tilde{u}_i}{\partial x_j} - \frac{\partial \tilde{u}_j}{\partial x_i}\right) = -\frac{1}{\rho}\frac{\partial \tilde{p}^*}{\partial x_i} - \frac{\partial \tau_{ij}}{\partial x_j} + F_i + F_i^t, \tag{2}$$

where $\tilde{u}_i$ is the resolved velocity with the tilde denoting a filtered quantity (u, v, and w are its components in the streamwise, cross-stream, and vertical directions, respectively); x_i is the position vector (x, y, and z are its components in the streamwise, cross-stream, and vertical directions, respectively); $\tilde{p}^*$ is a modified pressure that includes the resolved and subgrid scale turbulent kinetic energies (actual pressure will be denoted as p); F_i is a mean pressure gradient driving the flow and needed only in periodic simulations (for finite farm simulations, an imposed inflow drives the flow in the farm as detailed later); τ_{ij} is the deviatoric subgrid-scale stress tensor; and ${F_i}^t$ represents the aerodynamic forces of the turbine blades on the air (computed by the actuator line model; see details in Refs. [4,10]). These forces are computed using the local relative wind velocity for a given blade element and lift and drag coefficients that were determined experimentally for this VAWT model and used directly in our ALM-LES (see values of coefficients and other details in the original source [12]).

The tilde will be omitted hereafter for notational simplicity since only the resolved components of the variables are utilized. In addition, for the rest of this paper, an instantaneous turbulent parameter q is Reynolds decomposed into its mean Q (capitalized) and the perturbation q'. Time averaging is used as a surrogate for Reynolds averaging (due to the spatial heterogeneity of the mean flow) and is denoted by an overbar. We will often denote the Reynolds average of a mean quantity as $\overline{Q}$; the overbar here is redundant but adds clarity to some terms (for example, when a mean is multiplied by a Reynolds-averaged covariance, it is clearer to have an overbar over both). Spatial averages are taken either over some horizontal plane x-y or only in the cross-stream direction y; they will be denoted by angled brackets $\langle\rangle$ followed by the averaging direction(s) (e.g. $\langle \bar{Q} \rangle_y$ is averaged in time and over the cross-stream direction). All x-averaging for finite length farms is performed over the length of the farm only.

At the top boundary of the domain, zero vertical velocity (impermeable boundary) and zero shear stress are imposed. The bottom boundary is also impermeable, while the surface shear stress is imposed using an equilibrium log-law (since all flows are neutral) wall model with a wall roughness of $z_0 = 10^{-6}\, z_i$, where z_i is the depth of computational domain that is used to normalize all length scales in the code. The velocities in the code are normalized by the average friction velocity at the ground surface u_*. The horizontal boundary conditions are numerically periodic, but nonperiodic flows are simulated here using an inlet buffer region to model finite wind farms. A turbulent inflow is created for these simulations using a separate precursor periodic run (over flat terrain with the same z_0 but without turbines), and inflow planes are saved every five time steps. These planes are then interpolated within the five-time-step intervals and provided as inflow boundary conditions to the finite wind farms simulations at the downstream edge of the buffer zone. The two domains must thus have the same stream-normal (y-z) area and time step. The buffer zone spans the full width and height of the domain and extends across 20 streamwise grid nodes. In the buffer zone, the periodic inflow at the upstream edge is smoothly interpolated to the physically imposed precursor inflow at the downstream edge to avoid abrupt changes in the variables that cause the Gibbs phenomenon (spurious oscillations) with the spectral numerical methods [13]. The same LES code with the same numerical approaches and SGS model has been validated for a range of ABL flow regimes [14–16], and specifically for VAWTs under laboratory and field conditions [4,10]. No further validation is therefore presented here.

An important budget we examine in this paper is the one for the Reynolds-averaged (time-averaged here) MKE, which involves multiple terms reflecting the various mechanisms for generation, dissipation, and transport [17]. Since MKE is dominated by its streamwise component $U^2 (\gg V^2$ and $W^2)$, and since this is the main component extracted by wind turbines, it is more instructive to examine the budget equation of that component alone, which under steady-state conditions is given by

$$\underbrace{\frac{\partial\left(\frac{1}{2}\overline{U}^3\right)}{\partial x}}_{\text{I}} + \underbrace{\frac{\partial\left(\frac{1}{2}\overline{V}\,\overline{U}^2\right)}{\partial y}}_{\text{II}} + \underbrace{\frac{\partial\left(\frac{1}{2}\overline{W}\,\overline{U}^2\right)}{\partial z}}_{\text{III}}$$

$$= \underbrace{-\frac{\overline{U}}{\overline{\rho}}\frac{\partial \overline{p}}{\partial x}}_{\text{IV}} \underbrace{-\,\overline{U}\frac{\partial(\overline{u'u'})}{\partial x}}_{\text{V}} \underbrace{-\,\overline{U}\frac{\partial(\overline{u'v'})}{\partial y}}_{\text{VI}} \underbrace{-\,\overline{U}\frac{\partial(\overline{u'w'})}{\partial z}}_{\text{VII}} + \underbrace{\overline{U}\,\overline{F_x}}_{\text{VIII}} + \underbrace{\overline{U}\,\overline{F^t_x}}_{\text{IX}}. \tag{3}$$

In this equation, terms I to III represent the advection of streamwise MKE by the mean wind, term IV is a pressure interaction term that can be decomposed into a pressure transport and a redistribution to the other MKE components, and terms V, VI, and VII represent the interaction between the mean flow and turbulence. Term VIII is the generation of MKE by the imposed force driving the flow (here the large-scale pressure gradient) and is the only MKE input into the domain in periodic simulations, and IX is the interaction of the mean streamwise velocity and turbine forces that acts as a sink. If we consider a farm that is infinite in the cross-stream direction, the terms involving the mean cross stream velocity (V) and $\partial/\partial y$ (II and VI) can be neglected but are not exactly zero (they only redistribute energy within the farm but do not bring in new energy). Then, terms III and VII will dominate the vertical transport of MKE in and out of wind farms through the horizontal planes at the top and bottom of the farm where the vertical gradients are the largest. Term III is the vertical advection of MKE by mean vertical wind,$-0.5\,\overline{W}\,\overline{U}^2$, the spatial average of which also contains the so-called dispersive fluxes. Term VII is the turbulent flux of MKE arising from the interaction between mean flow and turbulence, $-\overline{u'w'}\,\overline{U}$. The first term in the equation dominates the horizontal influx of energy at the upstream plane of inflow to the farm. The eighth term is a significant source in periodic simulations of infinite farms where the flow is driven by a mean pressure gradient but is less significant in finite-fetch simulations. The ninth term is the extraction of MKE by the turbines (not all of which is converted to useful electricity)

III. SIMULATIONS SETUP

To investigate these streamwise MKE budget terms in VAWT farms, a suite of simulations was conducted. For finite-fetch wind farms, to be able to approach the fully developed wind farm boundary layer conditions near the end of the farm, long (in the streamwise direction) domains were used. One factor that constrains the size of the domain is the size of the wind turbine itself; the grid resolution should be fine enough to capture each turbine, while also allowing for a large domain size with a computable number of grid nodes. For these simulations, 9.1-m-tall wind turbines (blades start at 3 m above surface and are 6.1 m long) with a 1.2 m diameter were selected. The domain size we used for finite farms is 198 × 48 × 32 m, spanned by 660 × 160 × 336 grids in the x, y, and z directions, respectively. The grid resolution is thus $dx \times dy \times dz = 0.3 \times 0.3 \times 0.0955\,\text{m}$. This

TABLE I. Wind turbine configuration.

Number of blades per turbine N	3
Rotor diameter D	1.2 m
Blade vertical height H	6.1 m
Blade chord length c	0.11 m
Full turbine height	9.1 m
Airfoil section type	DU 06-W-200
Solidity $Nc/\pi D$	0.275
Tip speed ratio λ	2.18

implies that the turbine cross section is spanned by 4 × 4 grid points horizontally (reasonably close to the needed resolution as established in Ref. [10]). Our densest configuration has 12 turbines per row, each of which has a stream-normal are of $7.3\,\mathrm{m}^2$. Thus the maximum blockage ratio is about 5.7% of the y-z cross-sectional area of the domain, which is considered a safe blockage ratio that will not have an appreciable impact on the results [18]. Triangular VAWT clusters with a turbine spacing inside the cluster of $5D$ are used as the wind farm basic elements; this was found to be a near-optimal cluster design for energy production in previous work by the authors at sites with no dominant wind direction [4]. Four wind farm layouts with aligned and staggered clusters separated by $10D$ and $20D$ are simulated. The details of an individual wind turbine are shown in Table I (they can also be visualized in Fig. 1), while the layouts and wind farm simulations setups are detailed in Table II. For one of the cases, the $20D$-staggered wind farm, a longer domain with double the number of turbines was also simulated to investigate the influence of domain size and farm-fetch on the results more thoroughly (last column in Table II). Since the turbine diameter D and the distance between turbines within a cluster remain fixed, the only length scales that vary here are the distance between clusters $L(=10\,D$ or $20D)$ and the farm's total fetch L_f. Two dimensionless numbers hence control the dynamics: (1) D/L (1/10 or 1/20) and (2) $L_f/L =$ number of rows minus 1 $(N_r - 1)$. We will adopt L as the basic normalization length scale here. Physically, D/L modulates the energy recovery rate of the wake (a large D creates a larger wake that requires longer L to dissipate). $L_f/L = N_r - 1$ determines the relative size of the farm and whether it will reach the fully developed wind turbine array boundary layer (WTABL) regime or not (alternatively this can also be expressed as L_f/D).

For infinite wind farms, the setups are almost identical to the ones simulated previously by Hezaveh *et al.* [4], where periodic boundary conditions are used. The major difference is that since we aim to compare the results with finite wind farms, the pressure gradient is not augmented to compensate for the drag from turbines as done in our previous work. Therefore, only the $20D$-spacing periodic cases with aligned and staggered layouts can be simulated (in the $10D$-spacing simulations, the flow cannot be sustained without an augmented pressure gradient). The simulations setups for infinite wind farms are shown in Table III.

The simulations are first run for a warm up period of 100 000 time steps, and then the statistics are collected over 400 000 time steps, both with a time step $dt = 0.005\,\mathrm{s}$. This corresponds to about 30 eddy turnover times of statistical averaging, based on domain height and surface friction velocity. The turbines will in fact result in a faster turnover and this estimate is thus conservative. This was also confirmed by a checking the convergence of the time-averaged power production of each individual wind turbine to a constant value. The time-averaged three-dimensional flow field variables are outputted at the end of simulations.

IV. RESULTS AND DISCUSSION

A. Flow visualization

Figure 1 shows the streamwise velocity in the finite-fetch wind farms with $10D$ and $20D$ spacings, with aligned and staggered configurations. It is clear from this figure that the turbines

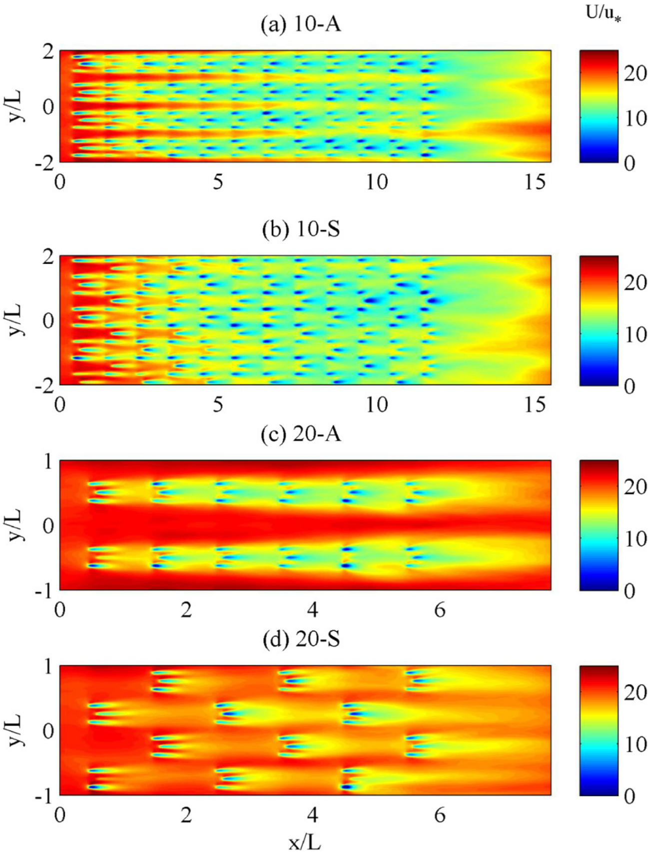

FIG. 1. Streamwise velocity slices (normalized by the friction velocity at the ground surface u_*) in finite-fetch wind farms with inflow for $10D$ and $20D$ horizontal spacings, mean wind from left to right: (a) $10D$ Aligned, (b) $10D$ Staggered, (c) $20D$ Aligned, (d) $20D$ Staggered.

in the $10D$-spacing cases, both aligned and staggered, are depressing the velocity within the wind farm more than the $20D$-spacing cases. The 20-A case maintains a high wind velocity in between each line of turbine clusters, while the velocity is reduced significantly in the wakes of the clusters. In the 10-A case, these corridors of higher velocity in between lines of clusters are only visible till the sixth row; after which the wakes generated by the turbine clusters merge. For both the 10-S and 20-S cases, except within the first row, such higher velocity corridors cannot be found due to the staggered layout. The important role played by the initial advective influx of MKE through

TABLE II. Finite wind farms layout configuration (S = staggered clusters; A = aligned clusters).

Simulation name	10-S and 10-A	20-S and 20-A	20-S-L
Cluster horizontal spacing ($L \times L$)	$10D \times 10D$	$20D \times 20D$	$20D \times 20D$
Wind farm layout	Staggered and aligned	Staggered and aligned	Staggered
Total number of turbines	144	36	72
Number of rows N_r	12	6	12
Number of clusters per row	4	2	2
Grid size $N_x \times N_y \times N_z$, nodes	$660 \times 160 \times 336$	$660 \times 160 \times 336$	$1140 \times 160 \times 336$
Domain size $L_x \times L_y \times L_z$, m	$198 \times 48 \times 32$	$198 \times 48 \times 32$	$342 \times 48 \times 32$

TABLE III. Infinite wind farms layout configuration with periodic domains.

Simulation name	20-S-P and 20-A-P
Clusters horizontal spacing ($L \times L$)	$20D \times 20D$
Wind farm layout	Staggered and aligned
Total number of turbines	24
Number of rows N_r	Infinite (four in the simulated domain)
Number of clusters per row	2
Grid size $N_x \times N_y \times N_z$, nodes	$320 \times 160 \times 336$
Domain size $L_x \times L_y \times L_z$, m	$96 \times 48 \times 32$

the frontal area, $0.5\overline{U}^3$, is clear in the 10-A simulations. It enables the higher velocity regions in between rows to persist till the sixth row and to serve as a source of MKE that can be transported laterally inside the farm. However, this initial influx seems to be exhausted beyond the sixth row, after which the downward entrainment of MKE from above would be expected to become important and to limit further reduction in the flow velocity (this will confirmed in later analyses). Recall that no mean pressure gradient is imposed in these simulations, and thus term VIII of Eq. (3) is small (a mean pressure gradient will form due to the action of the farm when an inflow is imposed). We also should point out here that the number of a given row is essentially the downstream distance from the beginning of the farm normalized by $L + 1$.

For the $20D$-spacing cases, we tested a longer domain length (20-S-L) to confirm the validity of the replenishment analyses that will follow and the insensitivity of the flow in the first rows to the total number of rows; its flow field is depicted in Fig. 2. After a streamwise distance equaling half of the fetch of the wind farm in the longer domain (six rows), the flow speed begins to plateau after a fast drop over the first few rows. If one considers the streamwise distance the flow has advanced inside the farm, that is the distance from the leading edge $x_f = x – x_{\text{first row}}$, then the number of a given row n is in fact a normalized quantity $n = x_f/L + 1$. It is hence plausible to expect some of the dynamics to scale with n. The $n = 6$ threshold in fact seems to be the value at which the flow equilibrates with the farm (see for 10-S, 10A, and 20-S-L; for 20-A and 20-S there are not enough rows to verify).

B. Streamwise MKE replenishment

We now turn our focus specifically to replenishment. Figure 3 shows the schematic view of a finite length wind-farm control volume. In this figure, the MKE advection through the frontal area [term I in Eq. (3)] and the upward-downward flux of MKE by mean advection (term III) and by turbulence (term VII) through the top and bottom planes of the wind farm are depicted. These are the main terms that dominate transport in and out of the whole farm volume as discussed above. The bottom plane here is the one that passes through the lower tip of the blades, while the top plane passes through the upper tip. The fluxes here are defined positive into the wind-farm control volume. The advective fluxes are visualized in Fig. 4, where the pseudocolor plot of MKE is overlaid on the streamlines plot. Figure 4(a), which shows the MKE x-y plane at midrotor height of the turbines,

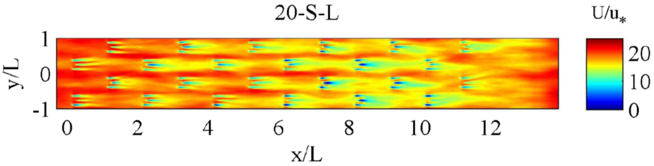

FIG. 2. Streamwise velocity (normalized by the friction velocity at the ground surface u_*) in the longer wind farm with inflow and $20D$ cluster spacings, case 20-S-L, mean wind from left to right.

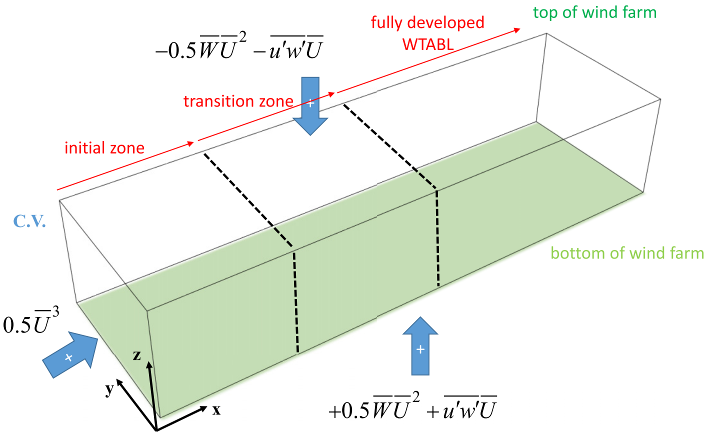

FIG. 3. Schematic view of a finite length wind-farm control volume; fluxes are defined positive into the control volume. WTABL is the "wind turbine array boundary layer." The control volume is overlaid on the plot shown in Fig. 4.

illustrates the MKE depletion when the flow enters the farm and the recovery downstream. Also visible is the cross-stream MKE advection in between the clusters [term II in Eq. (3)], but this causes only a redistribution inside the farm. Figure 4(b) is a x-z vertical plane that depicts how the slowdown of the flow in the farm generates an upward velocity. This upward motion advects MKE out of the top of the turbine domain [term III in Eq. (3)], which causes a net loss of MKE.

In Fig. 5 the spatially averaged vertical profiles of the turbulence-interaction transport of MKE (a), the downward advective transport of MKE (including by dispersion) (b), and the sum of these two fluxes (c) are shown. We show only the staggered cases since each aligned case had very similar profiles to the corresponding staggered one. Note that the spatial average of the vertical advection term encompasses the advection by the spatially averaged velocity and the so-called dispersive fluxes that arise from the spatial covariance of the time-averaged quantities [19,20]. For the 10-S,

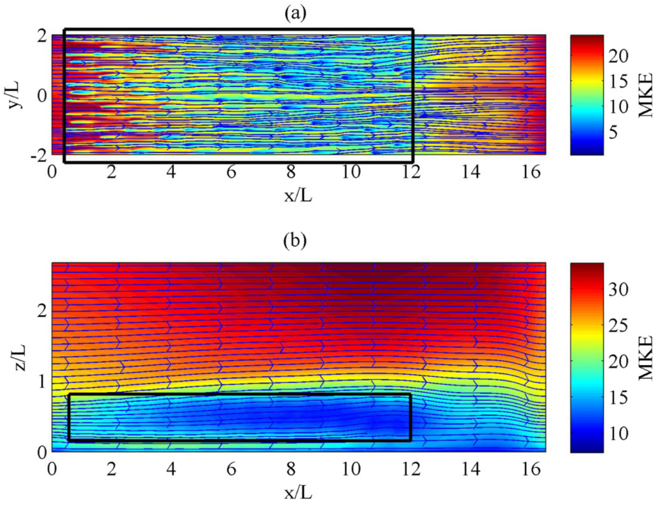

FIG. 4. 10-S case velocity streamlines overlaid on an MKE pseudocolor plot. (a) x-y plane at midheight of turbines and (b) x-z plane averaged in the y direction. The location of the wind farm and the control volume are delineated by the black rectangles.

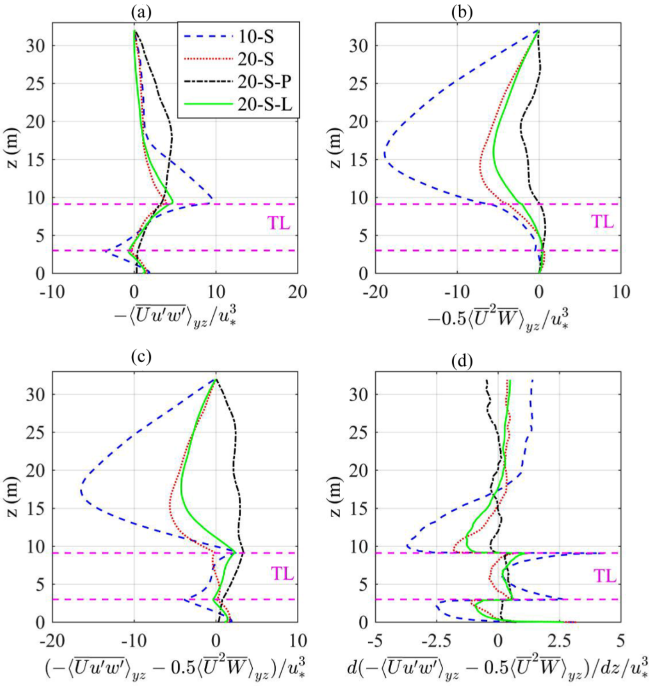

FIG. 5. Vertical profiles of fluxes of MKE averaged horizontally over the whole wind-farm domains: positive fluxes are downwards, negative are upwards. The turbine layer is delineated by the dashed magenta lines. (a) Turbulence interaction transport, (b) mean and dispersive transport, (c) total transport, (d) vertical gradient of total transport that shows the net total replenishment at a given height. As noted before, x-averaging is only over the farm length.

20-S, and 20-S-L cases, as illustrated in Fig. 5(b), the vertical advection of MKE is always negative for finite wind farms (given the definition we use with a negative sign implying an upward flux or loss). This confirms the result of Fig. 4(b): due to the reduction of streamwise wind velocity in the wind farm, the vertical velocity is predominantly upwards and is thus advecting MKE upwards and out of the wind-farm domain at the top. The advection is negative at the bottom also implying an upward flow that transports MKE into the turbine domain, but its magnitude is less than the outward flux at the top. The net effect of this advection is an MKE loss akin to a farm-scale Betz limit effect: as a streamtube approaches a farm, it must expand as the velocity slows down due to continuity, and there will necessarily be some losses related to this expansion.

The vertical profile of the interaction term between turbulence and the mean stream, $-\langle\overline{u'w'U}\rangle_{xy}$, is shown in Fig. 5(a). This transport is always positive (downward) at the top of the turbines, replenishing the turbine layer's MKE from above. For the 10-S case, there is a strong upward flux of energy from the bottom of the turbine blades (at 3 m, negative flux) as well as a downward flux from the top of wind farm (at 9.1 m, positive flux), both replenishing the turbine layer with MKE. For 20-S and 20-S-L cases, the fluxes are smaller at the bottom since the power extracted is less than for the 10-S case (due to the lower number of turbines per unit land area).

The sum of these two transport terms is shown in Fig. 5(c), which depicts a net downward flux over the whole wind farm from the top of the wind-farm domain (at 9.1 m), and for the 10-S case also an upward flux of energy from bottom of the wind-farm domain. The net flux is positive in all cases, indicating a net transport of MKE into the turbine layer, except the 20-S case, where it is slightly negative. The vertical derivatives of these fluxes are shown in (d); they reflect the net transport at any layer of height z (influx – efflux) and illustrate the positive supply rate of energy

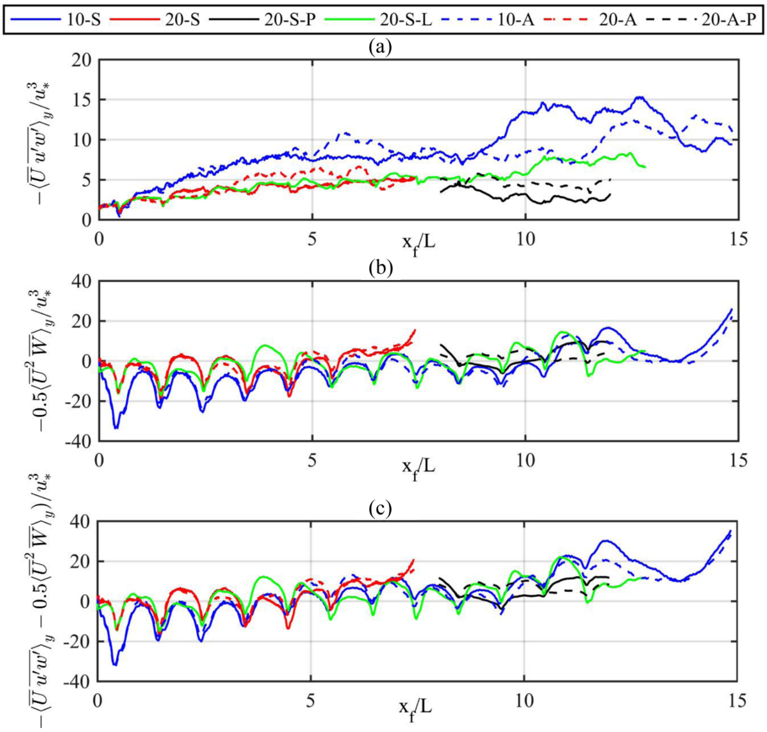

FIG. 6. Fluxes of MKE, averaged over the cross-stream y direction at top of wind farm, as a function of the distance from the leading edge of the farm x_f.

(positive derivative) all over the turbine layer. The only exception is the 20-S case where the net transport is ≈0; this configuration seems to be consuming only the energy advected at the upstream face of the control volume, and no appreciable replenishment occurs from the top or bottom.

In Fig. 5 the black line depicts the vertical profiles averaged in the x and y directions for the staggered periodic infinite-fetch wind farm with $20D$ horizontal cluster spacing. For both layouts (aligned case not shown but results are similar to staggered case) there is a downward flux of kinetic energy from interactions between mean flow and turbulence from aloft into the wind farm. However, in contrast to finite wind farms, there is little upward efflux of kinetic energy from vertical advection of MKE: that mean transport is much smaller for this case since $W \ll U$. In these wind farms, there is also no frontal advection of MKE available, and hence all the power transported to the wind-farm domain is thorough downward mean-turbulence interaction fluxes of kinetic energy. Naturally, these farms have a net flux of MKE into the turbine layer as illustrated in Fig. 5(d).

The farm averages of the replenishment terms presented above are instructive but do not inform on the evolution of the replenishment dynamics with distance from the leading edge. To investigate these MKE fluxes in more detail, we will now consider the streamwise variation of their averages in the y direction. The following analyses will focus on the top of the turbine layer since it is the primary replenishment boundary. The replenishment terms, at increasing streamwise distances from the leading edge, are depicted in Fig. 6 (ignore the periodic simulations for now). Over the length of the wind farm, there is a downward replenishment flux of energy from the interactions between turbulence and the mean flow, and an upward advective loss of MKE from the top of the finite-fetch wind farms. However, the net effect (sum) of these two terms shows net effluxes over the first few rows of clusters, and the switch to a net influx of MKE occurs later when the sum changes sign. That is, for the first few rows, not only are the turbines extracting MKE from the flow, but there is also a net loss of MKE by transport. For the 10-S and 10-A cases, the switch to net replenishment occurs about half way through the streamwise fetch of the wind farm, but for the 20-S and 20-A cases with the same domain length, this transition point is further downwind. The 20-S-L case (green line) is very similar to the 20-S over the first rows. After the midpoint of the 20-S-L wind farm, equivalent to the whole length of the 20-S case, this y-averaged total flux also becomes markedly positive, implying that MKE is being transported down into the turbine layer.

This will help us understand the relationship between cluster spacings and the needed length for the wind farm to reach the fully developed regime, where the dominant MKE transport mechanism is thorough downward interactions between mean and turbulence. The 20-S and the 20-S-L results for this replenishment, in Fig. 6(a), match quite well (although statistical convergence of each is not perfect) at all streamwise distances until the downwind edge of the shorter farm 20-S. Furthermore, the last row of the short case (20-S) is quite similar to the equivalent and subsequent rows in the 20-S-L case, suggesting that the fully developed (infinite) farm conditions are being approached towards the end of the 20-S case. The advective influx results [Fig. 6(b)] convey a similar picture overall, although they are more sensitive to acceleration of the flow in the last farm row.

To further probe this point, infinite wind farms fluxes (black lines in Fig. 6) are plotted from x_f/L of 8 to 12. These exact locations are irrelevant since these farms are periodic; the choice of the x_f location to plot them at is simply made to improve the figure visibility. As shown in this figure, the vertical fluxes patterns of the interaction between mean flow and turbulence in the infinite cases are indeed comparable with the last rows of clusters of finite wind farms (for both staggered and aligned configurations). They do not exactly match due to inconsistent normalization, a point we will come back to later. The reduction in the net vertical advective term (averaged over a row, for example) over the last rows in finite wind farms, and the fact that they approach the infinite farm results, also suggest that the flow is approaching the fully developed regime.

C. Energy extraction versus MKE replenishment

The available energy for extraction by the turbines is the sum of the frontal advected energy plus the replenished turbulent and mean or dispersive energy transported from the top and bottom of the turbine layer as analyzed in the previous subsection (for periodic simulation the power input by the driving pressure gradient is also important). The terms analyzed in these figures represent the fluxes of energy at the top and bottom planes (transport of energy per unit time per unit area, equivalent to power flow per unit area). To compare the influence of these fluxes to the frontal advective flux, one also needs to integrate over the unequal areas over which each of these fluxes acts to obtain the actual power inflows and outlfows at the different faces. These power flows can then be compared to the extracted power. Integrated up to some distance arbitrary x_f inside the farm ($x_f = 0$ is the upwind leading edge of the farm), these power flows are

$$P_{\text{Available}}(x_f) = P_{\text{Frontal}} + P_{\text{Top}}(x_f) - P_{\text{Bottom}}(x_f), \tag{4}$$

$$P_{\text{Frontal}} = \frac{1}{2}\rho \int_B^H L_y \langle \overline{U} \rangle_y{}^3 \, dz, \tag{5}$$

$$P_{\text{Top}}(x_f) = \rho \int_{x=0}^{x_f} L_y \left[(-\langle \overline{u'w'}\,\overline{U} \rangle_y) + \left(-\frac{1}{2} \langle \overline{W}\,\overline{U}^2 \rangle_y \right) \right]_{z=H} dx, \tag{6}$$

$$P_{\text{Bottom}}(x_f) = \rho \int_{x=0}^{x_f} L_y \left[(-\langle \overline{u'w'}\,\overline{U} \rangle_y) + \left(-\frac{1}{2} \langle \overline{WU}^2 \rangle_y \right) \right]_{z=B} dx, \tag{7}$$

$$\frac{dP_{\text{Available}}}{dx} = \frac{d[P_{\text{Top}}(x_f) - P_{\text{Bottom}}(x_f)]}{dx}, \tag{8}$$

where L_y is the width of the wind farm; H is the height of the top of the rotor blades and B the height of their lower tips; and ρ is the air density (our code solves for a normalized density of 1).

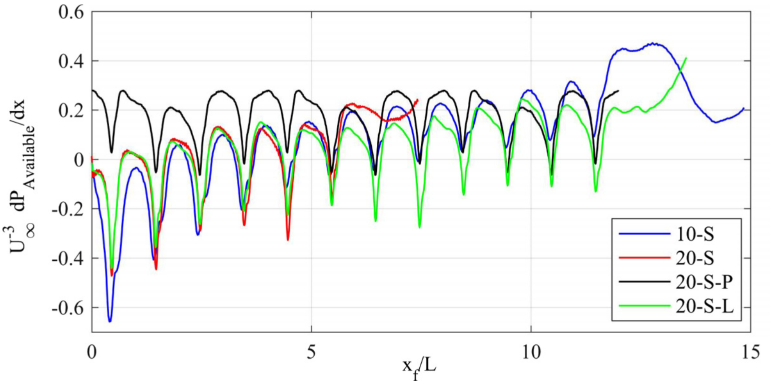

FIG. 7. Power replenishment from the top and bottom of wind farms for all staggered cases at a given streamwise point x_f. The streamwise distance is normalized by the distance between rows and as such is equal to the order of that row from the leading edge.

The local (in x) flux of replenished power as defined in Eq. (8) at a given downstream distance is shown in Fig. 7. Hereafter we normalize the results by U_∞ (taken before the last row at $z = 27.3$ m, which is three times the height of a VAWT) to be able to directly compare the finite and infinite wind farms since normalization with the friction velocity does not allow that. For the finite wind farms, the flux of power over the first four rows is predominantly negative, which as mentioned before shows that the MKE is being transported out of the control volume. However, the consistent normalization allows us to compare the 20-S-L and 20-S-P cases directly, making it clear that in terms of MKE replenishment the two become very similar over the last couple of rows of 20-S-L. This implies that equilibrium is not reached until row 10 of a finite farm. While the discussions in the previous sections suggested the flow approaches equilibrium by row 6, and indeed one can see a reduction in row-to-row streamwise variability after row 6, the replenishment seems to continue to evolve until row 10. The sudden increase in flux of replenished power after last row of clusters is due to sudden and large amount of energy transported downward. Since there is no more wind turbine drag in this region, the wind is accelerating in the x direction and creating a downward velocity, which brings significant amounts of MKE from aloft.

To focus on power production potential, we now consider the results averaged over the whole land area associated with a given row. Figure 8(a) shows the flux of replenished power due to vertical transport of MKE per row through the top and bottom; that is, the vertical flux of power from Eq. (8) is here x-integrated, but over each row individually from the midpoint to the upstream row to the midpoint to the downstream one. More simply this is $P_{\text{top}}{-}P_{\text{bottom}}$ from Eqs. (6) and (7) averaged over each row. This figure also confirms the previous observation that up to the third or fourth rows (depending on turbine density), the net power replenishment is negative, and that after the 10th row the 20-S-L case has similar values compared to the infinite wind farm replenished power. Figure 8(b) shows the extracted power per row in the wind farm. This is computed directly from the simulated lift force on each blade [10] and thus does not include energy losses to drag forces that do not generate power [that is, it is not equal to term IX in Eq. (3)]. The effect of initial frontal power is reflected in the high extracted power over the first five rows, but beyond the sixth row the net extracted power per row plateaus. The net extracted power for the 20-S-L and 20-S-P cases is comparable after the eighth row, which confirms that the primary source of power in the latter rows of the 20-S-L case is indeed the downward transport of MKE (the same as the 20-S-P) and that the effect of the frontal advection has been dissipated. The 10-S case has twice the number of turbines per row compared to the 20-S-L and 20-S-P cases; however, it is producing about the same amount of power compared to these two cases after the midpoint of these farms. This indicates that the 10-S configuration is not efficient in extracting more power. In fact, the figure reveals that by the last rows, when the effect of frontal advected power is lost, the extracted power [Fig. 8(b)]

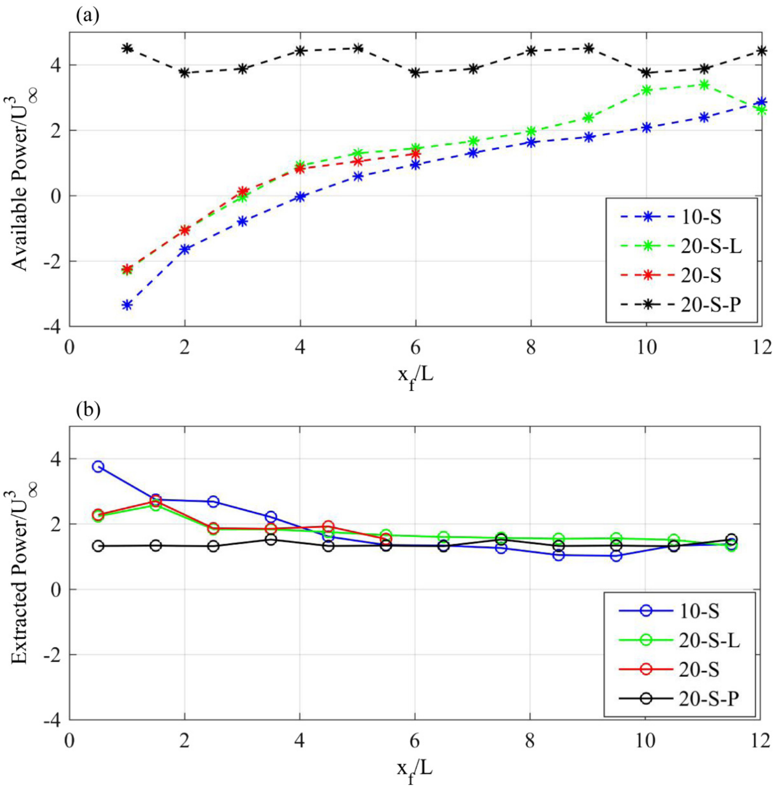

FIG. 8. Row-averaged replenishment of available (a) and extracted (b) power for all staggered cases. Markers are at location of each row of clusters. The streamwise distance is normalized by the distance between rows and as such is equal to the order of that row from the leading edge. The frontal flux is not included in (a).

in all configurations is about one third of the influx of replenished power [Fig. 8(a)]. This influx, rather than the number of turbines, thus controls the maximum produced power, and as shown in the figure, per row, the influx in the 10-S case is slightly inferior to the influx in the 20-S case.

Figure 9(a) shows the cumulative influx of available replenished power [Eq. (4) integrated from the leading edge to an arbitrary location x_f]. The value of the available power at $x_f = 0$ is simply P_{Frontal}, (zero for the periodic case) and changes after $x_f = 0$ are due to P_{Top} and P_{Bottom}. For all finite farms, up to the fifth row of turbines, the available power decreases (loss of energy by transport); the subsequent increase beyond row 5 marks the start of the regeneration (gain of energy by transport). For the $20D$-spacing cases, however, the initial decrease in total available power is lower than for the 10-S case in the upwind region of the farm, which can be attributed to the fact that the lower turbine density induces a weaker flow deceleration and therefore a smaller uplift associated with a positive W. This minimizes the loss of MKE through the advective or dispersive fluxes as shown in Fig. 6. The replenished power of the 20-S-L case is very similar to the 20-S case over the length of first half of the long wind farm and will also be similar for farms with fewer rows.

Figure 9(b) shows the cumulative extracted power up to a given row. The slope of the cumulative extracted power is larger in the first few rows of the 10-S case, which means they are producing more energy than subsequent rows. This is despite a net negative transport of energy (loss) out of the turbine layer over these initial rows, so the energy they extract is originating from P_{Frontal}. However, after the midpoint of the farm, this slope becomes smaller than the 20-S or 20-S-L cases and remains constant (i.e., subsequent rows extract a constant power) till the end of the wind farm. Except for the initial differences in power extraction in the first few rows, for all finite wind farms,

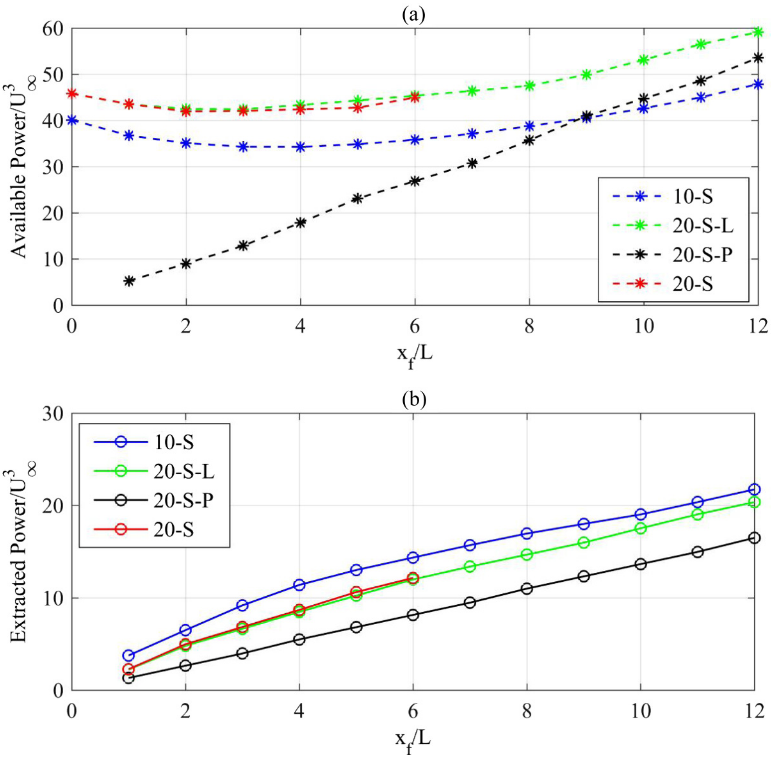

FIG. 9. Cumulative (a) replenished available and (b) extracted power for all staggered cases. Markers are at the location of each row of clusters.

the extracted power amounts are increasing with the same slope in the last rows. The extracted power over replenished power ratio is again about one third.

Figures 9(a) and 9(b) also show the replenished and extracted power for infinite wind farms. Since there is no frontal power available at infinite farms, the only source of power is from downward plan-form power from the top of wind farm. The figure illustrates that the power available in infinite wind farms is lower than finite farm till approximately row 6, after which the replenishment is very similar and so are the available replenished power levels. As a result, power production beyond row 6 of finite wind farms becomes equal to power production from infinite ones, as also illustrated in Fig. 8(b). However, the cumulative production remains about 25% lower at row 12 for the infinite farm since it did not benefit from the frontal advective influx that boosts production in the first four rows.

Figure 10 shows the average power coefficient C_p for each row of wind turbines in the finite wind farm simulations. C_P is defined as the power extracted by each row divided by the frontal equivalent wind power upstream of the whole farm for each row in the wind farm, excluding the space between turbines (that is, the denominator contains only the power in front of the turbines):

$$C_P = \frac{\sum_{n=1}^{N} P_{n,\text{Extracted}}}{\sum_{n=1}^{N} \frac{1}{2} \int_B^H \rho D \langle \overline{U} \rangle_D^3 \, dz}, \tag{9}$$

where N is the number of turbines per row and $\langle \overline{U} \rangle_D$ is the velocity upstream of the first row averaged over the diameter of the rotor D in the y direction. This figure confirms that the efficiency of the 20D staggered case in extracting energy from the available frontal power is much higher

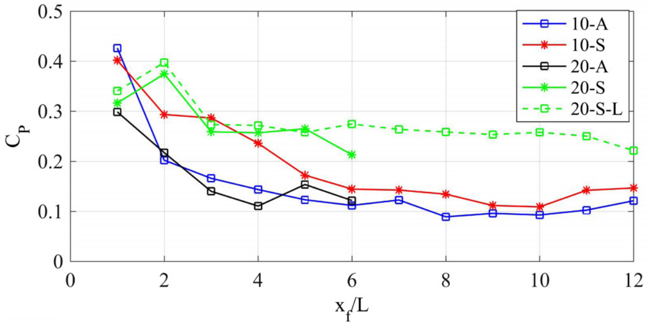

FIG. 10. Power coefficient C_P of each rows of clustered VAWT versus distance from leading edge, markers are at the location of each row of clusters.

than the $10D$ cases, although the $10D$ cases extract more total power. The C_P of the second row is higher than the first row in the $20D$ staggered cases due to higher velocity available from the flow constriction between the two upstream clusters. The longer $20D$ staggered wind farm is following the same trend as the shorter one, and after the sixth row its C_P becomes constant. Overall, the 10-S, 10-A, and 20-A are much less effective than the 20-S case, as expected.

V. DISCUSSION AND CONCLUSION

An ALM-LES model of vertical-axis wind turbines is used to study the MKE transport mechanisms into or out of a wind-farm domain consisting of three-turbine triangular clusters. Simulations over both finite fetch farms as well as infinite (periodic simulations) ones with similar configurations are conducted. Multiple configurations (staggered versus aligned) and cluster spacing ($10D$ and $20D$) in the farm are tested.

The first motivating question of the paper is: What transport mechanisms dominate the regeneration of MKE in VAWT wind farms, and how do they evolve with distance from the leading edge and with turbine density? For finite-fetch wind farms, the results indicate that there is a net downward turbulent flux of MKE from the top of the wind farm, but its magnitude is initially smaller than the net upward vertical advective efflux resulting from the upward velocity that is generated by the slowing down of the flow in the farm. Short farms thus lose energy over a significant fraction of their fetch, about six rows for the setups studies here, by efflux. Further downwind, as the local Reynolds-averaged vertical velocity W is reduced, turbulent replenishment becomes dominant, and we observe a net influx of MKE into the turbine layer. For the longer finite-fetch farm with $20D$ staggered configuration, the results confirm a significant net replenishment of MKE into the farm for the latter rows.

The second motivating question is: How large should VAWT wind farms be to display the dynamics of fully developed (infinite) wind-turbine array boundary layers? The answer is not very large. We observe that the switch from net loss to net replenishment in finite farms seems to occur around the sixth row in all configurations considered, and that beyond the eighth row the power extraction as well as the replenishment in the finite and infinite farms, per row, become very similar. Revisiting Fig. 3, the results thus indicate that the initial adaptation zone is about six rows, followed by a short transition zone of two to four rows, and beyond that the flow regime and farm performance seem to mimic an infinite farm in a fully developed WTABL. These zones are in fact quite similar to the ones suggested for air flow entering an urban canopy. Belcher *et al.* [21] for urban flows identified what they called an impact region in which the sudden flow deceleration due to the roughness element drag dominates the dynamics. This is followed by an adjustment region where the flow evolves until the drag of the canopy and the downward momentum transport are balanced. Finally, a region exists where the flow near the canopy is in equilibrium with the underlying surface, but the upper layers of the ABL are adapting to the change in roughness. These three zones are very similar to the ones we observe here: over the first six rows the mean flow adapts to the surface change [notice, for example, in Fig. 6(b) that the mean and dispersive advective fluxes becomes self-similar for rows beyond six], over the next two to four rows the turbulence adapts (notice, for example, that the 20-S-L and 20-S-P simulations do not become fully similar till row 10 in Fig. 7), and beyond that the dynamics are similar to a WTABL. The farm flow thus bears similarities to other canopy flows over an urban or vegetated surface.

A question that arises is whether these results, expressed in terms of the row number, are generalizable. The length scales of physical relevance that one can use to normalize the distance into the farm x_f are the interrow spacing L that we adopt, the turbine diameter D (or the proportional interturbine spacing within the cluster), and the ABL depth z_i. Since we did not vary D and z_i, the present results cannot inform us on the influence of these two parameters. However, our normalization with $L(x_f/L = \text{row number} + 1)$ did result in reasonable similarity in the forms of the various farm configuration results (L varies by a factor of two), although exact collapse requires deeper domains to be able to normalize by a constant velocity. This confirms that when D and z_i are kept constant, normalization with L does result in flow similarity. This conclusion can again be made by analogy to flow adjustment in urban terrain. Belcher *et al.* [21] found the adjustment length to depend on the reciprocal of the roughness element density, which for wind farms $\sim 1/L^2$, and thus L is a relevant normalization scale. However, they also found that the adjustment length depends on the drag coefficient of the roughness elements, which for wind turbines would scale with the frontal area. Therefore, to develop a universal scaling one needs to also vary D and maybe develop a formulation of the adjustment length in wind farms that simultaneous accounts for D and L, but this is beyond the scope of this paper. The ABL height z_i will also become a relevant scale for very large farms when the WTABL extends all the way to z_i.

Despite the adjustment over 6 to 10 rows, finite wind farms simulations also show that the role of the initial streamwise advective influx for the total farm power output remains significant. It provides a generation boost for the initial rows that maintains the farm generation higher than an equivalent collection of turbines in an infinite farm [finite farm production over 12 rows was about 25% higher than for an infinite farm, Fig. 9(b)].

For the downwind rows, it was also clear that a spacing of $10D$ is too limiting. The MKE replenishment rather than the number of clusters control power production beyond about row 6, and the closer spacing of clusters did not significantly increase that replenishment. Thus a $10D$-spacing farm produces about the same amount of total power as a $20D$-spacing farm in the latter rows, despite having four times as many turbines, and thus has about half the efficiency. Staggered configurations, as expected, are more efficient than aligned ones.

A primary farm design lesson from the results is that the layout should focus on maximizing replenishment, which for example might be achieved better using irregular layouts. Cluster designs can be beneficial for VAWTs, but equivalent results for HAWTs are not available. In addition, the dense farms were losing a significant amount of MKE initially by vertical advection. Therefore, farms that have a low initial density might be more favorable since they extract the power more gradually, minimize the slowdown, and avoid the loss of MKE over the first few rows. To summarize, given that the large majority of wind-farm studies consider staggered or aligned configurations, researchers should experiment more with unconventional and irregular farm layouts since the potential for improved overall farm performance beyond the conventional layouts exists.

ACKNOWLEDGMENTS

This work was supported by the Siebel Energy Challenge and the Andlinger Centre for Energy and the Environment of Princeton University. The simulations were performed on the supercomputing clusters of the National Centre for Atmospheric Research through Projects No. P36861020 and No. UPRI0007 and of Princeton University.

[1] D. J. McKay, *Sustainable Energy—Without the Hot Air*, https://www.withouthotair.com (2008).

[2] F. Breu, S. Guggenbichler, and J. Wollmann, *20% Wind Energy by 2030 Increasing Wind Energy's Contribution to U.S. Electricity Supply* (NREL, 2008), https://www.nrel.gov/docs/fy08osti/41869.pdf.

[3] J. O. Dabiri, Potential order-of-magnitude enhancement of wind farm power density via counter-rotating vertical-axis wind turbine arrays, J. Renew. Sustain. Energy **3**, 043104 (2011).

[4] S. H. Hezaveh, E. Bou-Zeid, J. O. Dabiri, M. Kinzel, G. Cortina, and L. Martinelli, Increasing VAWT wind farm power density using synergistic clustering, BLM 1 (2018).

[5] M. Calaf, C. Meneveau, and J. Meyers, Large eddy simulation study of fully developed wind-turbine array boundary layers, Phys. Fluids **22**, 015110 (2010).

[6] M. Calaf, M. B. Parlange, and C. Meneveau, Large eddy simulation study of scalar transport in fully developed wind-turbine array boundary layers, Phys. Fluids **23**, 126603 (2011).

[7] J. Meyers and C. Meneveau, Large eddy simulations of large wind-turbine arrays in the atmospheric boundary layer, in *Proceedings of 48th AIAA Aerospace Sciences Meeting Including the New Horizons Forum and Aerospace Exposition, Orlando, Florida* (AIAA, Reston, VA, 2010), AIAA 2010-827.

[8] J. Meyers and C. Meneveau, Optimal turbine spacing in fully developed wind farm boundary layers, Wind Energy **15**, 305 (2012).

[9] M. Kinzel, D. B. Araya, and J. O. Dabiri, Turbulence in vertical axis wind turbine canopies, Phys. Fluids **27**, 115102 (2015).

[10] S. H. Hezaveh, E. Bou-Zeid, M. W. Lohry, and L. Martinelli, Simulation and wake analysis of a single vertical axis wind turbine, Wind Energy **20**, 713 (2016).

[11] E. Bou-Zeid, C. Meneveau, and M. Parlange, A scale-dependent Lagrangian dynamic model for large eddy simulation of complex turbulent flows, Phys. Fluids **17**, 025105 (2005).

[12] M. C. Claessens, The design and testing of airfoils for application in small vertical axis wind turbines, Master's thesis, McMaster University, 2006.

[13] Q. Li, E. Bou-Zeid, and W. Anderson, The impact and treatment of the Gibbs phenomenon in immersed boundary method simulations of momentum and scalar transport, J. Comput. Phys. **310**, 237 (2016).

[14] V. Kumar, J. Kleissl, C. Meneveau, and M. B. Parlange, Large-eddy simulation of a diurnal cycle of the atmospheric boundary layer: Atmospheric stability and scaling issues, Water Resour. Res. **42**, W06D09 (2006).

[15] W. Yue, C. Meneveau, M. B. Parlange, W. Zhu, H. S. Kang, and J. Katz, Turbulent kinetic energy budgets in a model canopy: Comparisons between LES and wind-tunnel experiments, Environ. Fluid Mech. **8**, 73 (2008).

[16] J. Huang and E. Bou-Zeid, Turbulence and vertical fluxes in the stable atmospheric boundary layer. Part I: A large-eddy simulation study, J. Atmos. Sci. **70**, 1513 (2013).

[17] R. B. Stull, *An Introduction to Boundary Layer Meteorology* (Springer, New York, 1988).

[18] H. Sarlak, T. Nishino, L. A. Martínez-Tossas, C. Meneveau, and J. N. Sørensen, Assessment of blockage effects on the wake characteristics and power of wind turbines, Renew. Energy **93**, 340 (2016).

[19] M. R. Raupach and R. H. Shaw, Averaging procedures for flow within vegetation canopies, Boundary-Layer Meteorol. **22**, 79 (1982).

[20] D. Poggi and G. G. Katul, Micro- and macro-dispersive fluxes in canopy flows, Acta Geophys. **56**, 778 (2008).

[21] S. E. Belcher, N. Jerram, and J. C. R. Hunt, Adjustment of a turbulent boundary layer to a canopy of roughness elements, J. Fluid Mech. **488**, 369 (2003).